Physics Contribution

Bioluminescence Tomography—Guided Radiation Therapy for Preclinical Research

CrossMark

Bin Zhang, PhD,* Ken Kang-Hsin Wang, PhD,* Jingjing Yu, PhD,*,†
Sohrab Eslami, PhD,‡ Iulian Iordachita, PhD,‡ Juvenal Reyes, MD,*
Reem Malek, PhD,* Phuoc T. Tran, MD, PhD,*,§
Michael S. Patterson, PhD,‖ and John W. Wong, PhD***

*Department of Radiation Oncology and Molecular Radiation Sciences, Johns Hopkins School of
Medicine, Baltimore, Maryland; †School of Physics and Information Technology, Shaanxi Normal
University, Shaanxi, China; ‡Laboratory for Computational Sensing and Robotics, Johns Hopkins
University, Baltimore, Maryland; §Department of Oncology and Urology, Brady Urological Institute,
Johns Hopkins University, Baltimore, Maryland; and ‖Department of Medical Physics and Applied
Radiation Sciences, McMaster University, Hamilton, Ontario, Canada

Summary

To overcome the limitations of cone beam computed tomography (CBCT) in localizing soft tissue targets, we developed online 3D bioluminescence tomography (BLT) for the small animal radiation platform. The optical system is capable of locating a target's center of mass with an average accuracy of 1 mm. The integrated online BLT/CBCT system provides an effective

Purpose: In preclinical radiation research, it is challenging to localize soft tissue targets based on cone beam computed tomography (CBCT) guidance. As a more effective method to localize soft tissue targets, we developed an online bioluminescence tomography (BLT) system for small-animal radiation research platform (SARRP). We demonstrated BLT-guided radiation therapy and validated targeting accuracy based on a newly developed reconstruction algorithm.

Methods and Materials: The BLT system was designed to dock with the SARRP for image acquisition and to be detached before radiation delivery. A 3-mirror system was devised to reflect the bioluminescence emitted from the subject to a stationary charge-coupled device (CCD) camera. Multispectral BLT and the incomplete variables truncated conjugate gradient method with a permissible region shrinking strategy were used as the optimization scheme to reconstruct bioluminescent source distributions. To validate BLT targeting accuracy, a small cylindrical light source with high CBCT contrast was placed in a phantom and also in the abdomen of a mouse carcass. The center of mass (CoM) of the source was recovered from BLT and used to guide radiation delivery. The accuracy of the BLT-guided targeting

solution for soft tissue targeting, particularly for small, nonpalpable, or orthotic tumor models.

was validated with films and compared with the CBCT-guided delivery. In vivo experiments were conducted to demonstrate BLT localization capability for various source geometries.

Results: Online BLT was able to recover the CoM of the embedded light source with an average accuracy of 1 mm compared to that with CBCT localization. Differences between BLT- and CBCT-guided irradiation shown on the films were consistent with the source localization revealed in the BLT and CBCT images. In vivo results demonstrated that our BLT system could potentially be applied for multiple targets and tumors.

Conclusions: The online BLT/CBCT/SARRP system provides an effective solution for soft tissue targeting, particularly for small, nonpalpable, or orthotopic tumor models.

Introduction

In radiation therapy, studies in small animal models are a key means to understand and develop treatments for a wide spectrum of diseases (1, 2). Several groups, including ours, have initiated efforts to develop small-animal irradiators that mimic human treatment (3-12). In these systems, on-board computed tomography (CT) and cone-beam CT (CBCT) are used to guide radiation therapy. Our small-animal radiation research platform (SARRP) (4, 13) uses CBCT to guide focal irradiation that is accurate to within 0.2 mm.

Although our experience and that of other investigators has shown that CT or CBCT is invaluable for guiding focal irradiation (6, 7, 14-16), localization of low contrast and small soft tissue targets remains challenging. Presently, micro-magnetic resonance imaging, micro-positron emission tomography, and micro-single photon emission CT are the more common modalities that can provide improved localization accuracy for soft tissue targets (17). Cost, shielding, and space limitations of existing irradiators are all obstacles preventing implementation of these modalities. A compelling solution is molecular optical imaging, which has a compact footprint, costs less, and does not use ionizing radiation.

Among possible optical modalities, bioluminescence imaging (BLI) has found extensive applications (18-21) and is almost free of background noise. Due to the nonlinear relationships among signal strength, surface emittance, and tissue optical properties, 2-dimensional (2D) BLI measured on the object's surface is limited in its ability to accurately localize a target in 3D. It has been shown, however, that with sophisticated reconstruction algorithms and mathematical models of light transport inside tissue, bioluminescence tomography (BLT) based on 2D BLI can reveal 3D distribution of internal bioluminescent sources (22-27). With the wide availability of genetically engineered mouse models in oncologic and radiation biology research, we propose BLT as an attractive solution for soft tissue targeting, which can be readily applied to existing animal models.

We previously built an integrated CBCT/BLT system in a stand-alone configuration (28) for development of calibration methods and reconstruction algorithm. In the current study, we introduced an online BLT/CBCT system for the SARRP and a significantly improved BLT algorithm. Because of the online design, we were able to demonstrate BLT-guided radiation therapy using the SARRP for the first time. Multispectral BLT (29), inverse calculation using the incomplete variables truncated conjugate gradient (IVTCG) method (30) and a permissible region-shrinking strategy (31) were combined to enable fast and accurate BLT reconstruction. Studies were performed in a phantom and mouse carcasses with an implanted light source to show the capability of BLT-guided radiation therapy. In vivo experiments were conducted to demonstrate the potentiality of applying the BLT system for multiple targets and tumors.

Methods and Materials

SARRP optical system

The second-generation SARRP allows 360° isocentric gantry rotation and is equipped with CBCT and robotically controlled stages for animal positioning (4, 13). For CBCT imaging, a 20.5×20.5 cm^2 amorphous silicon flat panel detector with 200-µm pixel pitch (Perkin-Elmer, Waltham, MA) is used to acquire 65-kVp x-ray projection images from a 0.4-mm focal spot. Figure 1a shows the BLT system consisting of a camera-filter-mirror assembly docked with the SARRP. A rotating 3-mirror system directs light emitted from the object to a stationary charge-coupled device (CCD) camera and supports multi-view imaging (Fig. 1b). The optical path from the SARRP isocenter through the 3 mirrors to the lens front surface is 42 cm, and the depth of field is 4 cm. Figure 1c illustrates the side view of the SARRP-BLT system. A light-tight dome covers the mirror and object. The CCD camera has a 27.6×27.6 mm^2 back-illuminated sensor with 2048×2048 pixels (or 13.5 µm/pixel) (iKon-L 936; Andor Technology, Belfast, UK) and is fitted with a 35-mm f/1.4 lens (Rokinon, New York, NY) for optical
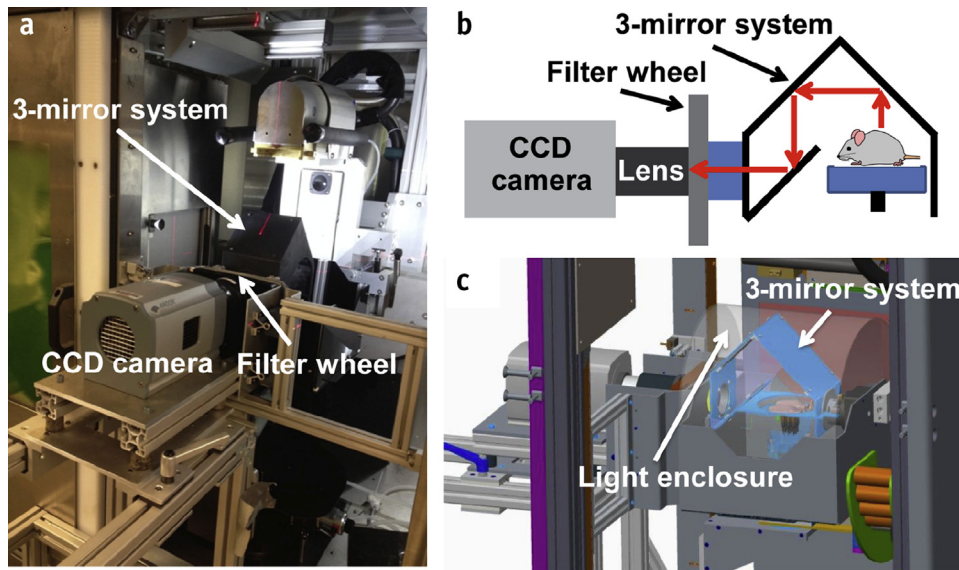
Fig. 1. (a) Online BLT/SARRP system. (b) Optical path from object to lens. (c) Light enclosure to cover the object and mirror assembly. *Abbreviations:* BLT = bioluminescence tomography; CCD = charge-coupled device; SARRP = small animal radiation research platform.

image acquisition. The quantum efficiency of the CCD sensor is >90% over a wavelength range of 500 to 700 nm. The camera operates at −80°C to minimize dark current and other thermal noise during image acquisition. Spectral discrimination is provided by 4 band-pass filters (590, 610, 630, and 650 nm and 10-nm full width half maximum [FWHM]; Andover, Salem, NH) mounted in a computer-controlled wheel (Edmund Optics, Barrington, NJ). The procedures for calibrating the intensity nonuniformity arising from the lens vignetting effect and nonuniform pixel response of the CCD chip are described in the Supplementary Material Section E1 (available online at www.redjournal.org).

BLT reconstruction

Diffusion approximation (DA) of the radiation transport equation is widely used to model light propagation in tissue when photon transport is dominated by scattering (32). In the continuous wave mode, the DA and the Robin-type boundary condition are expressed as

$$\begin{cases} -\nabla \cdot D(r)\nabla \Phi(r) + \mu_a(r)\Phi(r) = S(r), \ r \in \Omega \\ \Phi(\xi) + 2A\hat{n} \cdot D(\xi)\nabla \Phi(\xi) = 0, \ \xi \in \partial\Omega \end{cases} \quad (1)$$

where $\Phi(r)$ is the photon fluence rate at location r in domain Ω; $D(r) = 1/(3(\mu_a + \mu'_s))$ is the diffusion coefficient; and μ_a and μ'_s are absorption and reduced scattering coefficients, respectively; and $S(r)$ is the bioluminescence source distribution. ξ represents points on the object boundary, and coefficient A can be derived from Fresnel's law (33), depending on the refractive index of tissue and air. $\hat{n}$ is the unit vector pointing outward, normal to the boundary $\partial\Omega$.

Eq 1 can be further expressed in the form of Green's functions, which link the fluence rate at the object boundary and the bioluminescence source distribution (34, 35). For M measurements and N mesh nodes, the relationship can be expressed as

$$\begin{bmatrix} \varphi_1 \\ \vdots \\ \varphi_M \end{bmatrix} = \begin{bmatrix} G_{1,1} & \cdots & G_{1,N} \\ \vdots & \ddots & \vdots \\ G_{M,1} & \cdots & G_{M,N} \end{bmatrix} \begin{bmatrix} s_1 \\ \vdots \\ s_N \end{bmatrix} \quad (2)$$

where $[\varphi_1, ..., \varphi_M]^T$ is a vector containing the fluence rate measured at the boundary, $[s_1, ..., s_N]^T$ is the vector of unknown bioluminescence distribution, and $G_{i,j}$ is the Green's function describing the relationship between the fluence rate φ_i at detector i on the surface and the source s_j at node j.

Multispectral images were acquired to improve BLT reconstruction results (24, 29). Eq 2 can be rewritten as

$$\begin{bmatrix} \varphi(\lambda_1) \\ \vdots \\ \varphi(\lambda_k) \end{bmatrix} = \begin{bmatrix} \eta(\lambda_1)G(\lambda_1) \\ \vdots \\ \eta(\lambda_k)G(\lambda_k) \end{bmatrix} [s]$$
$$\varphi = \widetilde{G}s \quad (3)$$

where $G(\lambda_k)$ is Green's function, extended from Eq 2 at wavelength λ_k, and $\eta(\lambda_k)$ is the relative spectral weight that accounts for the source emission spectrum, the transmission of individual filters, and the CCD quantum efficiency at different wavelengths. A modified version of the open source NIRFAST software (http://www.dartmouth.edu/~nir/nirfast/) (33, 36) was used to generate the Green's function. To avoid biasing the reconstruction algorithm by the larger signals at longer wavelength (due to lower attenuation) (27), the measurement φ and the weighted

Green's function $\widetilde{G}$ at each wavelength were divided by the maximum value of the measurement φ, that is,

$$\begin{cases} \overline{\varphi}(\lambda_k) = \varphi(\lambda_k)/\max(\varphi(\lambda_k)) \\ \overline{G}(\lambda_k) = \widetilde{G}(\lambda_k)/\max(\varphi(\lambda_k)) \end{cases} \quad (4)$$

Our approach to reconstructing the bioluminescence source distributions was to minimize the deviation between the computed $\overline{G}$ s and measured fluence rate $\overline{\varphi}$ at the object boundary. However, the BLT reconstruction is ill-posed and underdetermined with fewer measurements than unknowns. He et al (30) introduced the IVTCG optimization algorithm and demonstrated that this algorithm can stably solve this minimization problem with an L1 regularization term. BLT minimization is given as

$$\min_s \frac{1}{2}\left\|\overline{G}s - \overline{\varphi}\right\|_2^2 + \tau\|s\|_1 \quad (5)$$

where τ is a non-negative regularization parameter, $\|\cdot\|_2^2$ denotes the square of the Euclidean norm, such as $\sum_i (\overline{G}s - \overline{\varphi})_i^2$, and $\|s\|_1 = \sum_i |s_i|$ is the L1 norm of s. We used the finite element method, where the imaging object was discretized into a 3D mesh from the SARRP CBCT as the framework on which to numerically build the Green's function and system matrix.

To improve convergence and reduce computation time, an iterative strategy was chosen to adaptively shrink the solution space (31). The initial permissible solution space is the whole mesh domain except for the surface nodes. The permissible region reduction factor is defined as $\beta = (N_1/N_f)^{1/(N_{it}-1)}$, where N_1 is the initial number of nodes for the permissible region. In this study, the number of iterations, N_{it}, was set to 20 and included all possible solutions; the final number of nodes (N_f) was set to 1. The objective function

$$f_i = \sum \left\|\overline{G}s^{(i)} - \overline{\varphi}\right\|_1 \quad (6)$$

was calculated according to the reconstructed source distribution $s^{(i)}$ at the ith iteration. The permissible region was shrunk at each iteration by first sorting the nodes in descending order of source strength and then selecting the nodes with high average source strength per 1 mm^3 volume until the number of nodes was equal to N_R/β, where N_R is the total number of nodes in the permissible region. The solution corresponding to the minimum of the objective function was selected. In this study, counts per pixel area were chosen as the measurement quantity at the boundary and were not linked to absolute emittance. Further study to calibrate CCD counts to absolute emittance at the boundary is warranted (28). The optical and reconstruction parameters used in this study are listed in Table E1 (available online at www.redjournal.org). A threshold 10% of the maximum source strength was applied for display of the BLT results shown in this work.
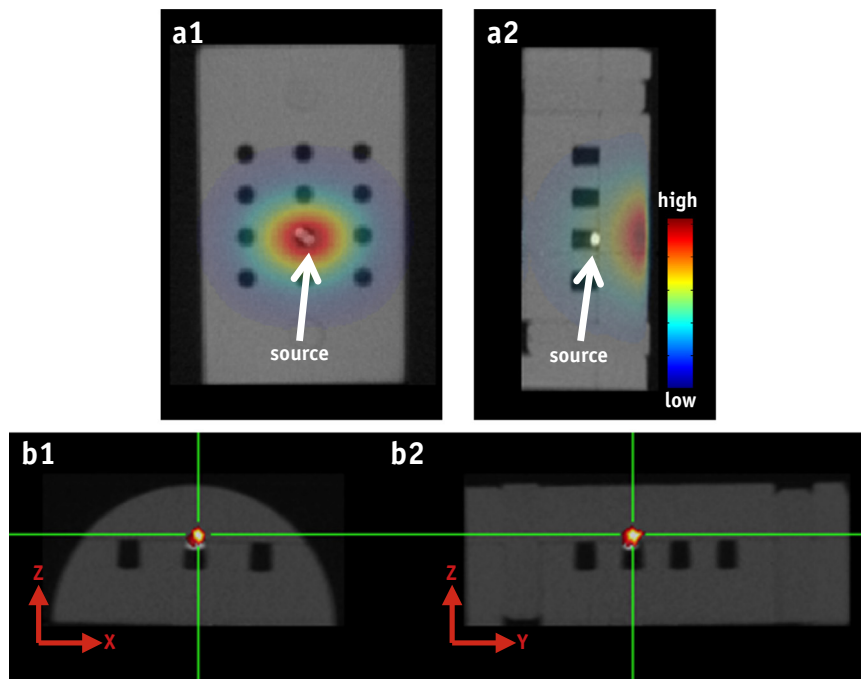

Fig. 2. (a1, a2) AP and lateral BLI overlaid with the CBCT of the phantom (half cylinder, 30-mm diameter × 41-mm height), which also shows the embedded light source. (b1, b2). The transverse and sagittal views of BLT slices overlaid with CBCT. The cross depicts the CoM of reconstructed bioluminescent source. *Abbreviations:* AP = anteroposterior; BLI = bioluminescence imaging; CBCT = cone beam computed tomography; CoM = center of mass. Other abbreviations as in Fig. 1.

BLT-guided irradiation

The workflow of online BLT-guided irradiation is as follows: (*1*) dock the BLT system with the SARRP; (*2*) perform geometry calibration, mapping the BLI coordinates to the CBCT coordinates (see Supplementary section E1 for details of the calibration procedures; available online at www.redjournal.org); (*3*) acquire multispectral BLI; (*4*) detach the BLT system and acquire object CBCT; and (*5*) use NIRFAST software to generate the 3D mesh of the object from CBCT and map the multispectral BLI to the mesh surface based on the geometry calibration. The 3D distribution of the bioluminescence source is then reconstructed, and the center of mass (CoM) of the reconstructed source is calculated for radiation guidance. Total experiment time was approximately 40 min/animal. In this study, the CBCT volume was reconstructed with a voxel resolution of 0.2 to 0.25 mm^3. Multispectral BLI were acquired at wavelengths of 590, 610, 630, and 650 nm with 0.6 mm/pixel. Although our system is capable of acquiring multiple projections of BLI by rotating the mirror assembly, single-view BLI was used for the 3D reconstruction in this study. For BLT-guided experiments, the mesh was set at approximately 10,000 nodes and 60,000 tetrahedral elements, and the element size varied between 0.1 and 0.5 mm^3.

To assess BLT targeting accuracy, we performed experiments using a tissue-simulating phantom and mouse carcasses. A cylindrical self-illuminated light source (tritium gas, 12-year half-life unit; Trigalight; Mb-microtec Ag, Niederwangen, Switzerland) with high CBCT contrast, 0.9-mm diameter × 2-mm length was placed inside the phantom as well as in the carcass' abdomen. The mouse was euthanized just prior to Trigalight implantation and shaved for BLT measurement. The relative spectral weights of the source were 0.90, 1, 0.95, and 0.55 at wavelengths 590, 610, 630, and 650 nm, respectively. Methods of phantom fabrication and measurements of optical properties were published previously (37). The mouse carcass was assumed to be optically homogeneous. To determine the optimal optical properties, several sets of optical properties from published reports (38-41) were initially tested by comparing the CoM of the reconstructed Trigalight in one carcass to that obtained by CBCT. Once the optimal values were determined, the same optical properties were applied to all carcasses. Gafchromic EBT3 film (Ashland, Covington, KY) was used to verify targeting accuracy for an anteroposterior (AP) and lateral delivery by placing the film on the beam exit sides of the phantom and carcass. Details of the film measurements can be found in the Supplementary Section E2 (available online at www. redjournal.org). The source centroid position revealed from CBCT was regarded as the ground truth for target position. Both BLT- and CBCT-guided irradiation were performed and compared.

In vivo BLT study

To assess the capability of our BLT system for multiple sources and for tumors, 2 in vivo experiments were conducted. For the first experiment, 2 larger cylindrical Trigalight sources (2-mm diameter × 6-mm length) were surgically implanted in the abdomen of a mouse and were imaged with the BLT system. For the second experiment, a mouse bearing a subcutaneous tumor, firefly PC3-Luc prostate cancer cells, in the lower dorsal region was imaged. Details of the in vivo experiments can be found in Supplementary Section E3 (available online at www .redjournal.org).

Results

Phantom experiments

The Trigalight source was placed in 1 of the holes of the phantom (Fig. 2a1). A small piece of polystyrene foam (Styrofoam) was inserted underneath the source to mini-
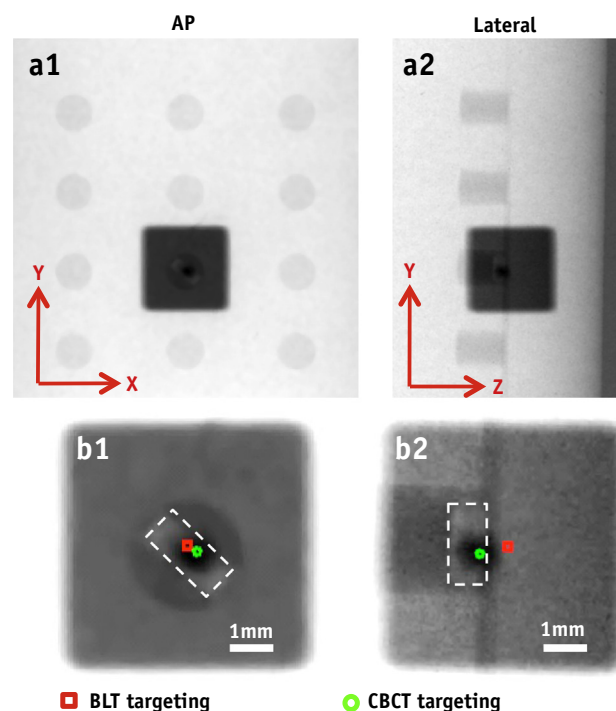

Fig. 3. Film results of target validation in phantom: The BLT-guided radiation was delivered with a 5-mm × 5-mm beam; CBCT guidance with a 0.5-mm-diameter beam. (a1,a2) Results in the AP and lateral views. (b1, b2) Corresponding enlarged views. The true source was contoured by the dashed line. The green circle marks the center of the CBCT-guided radiation; red square marks the center of the BLT-guided radiation. Abbreviations as in Fig. 1. A color version of this figure is available at www.redjournal.org.

mize the air gap between source and detector points at the phantom surface. Note that the strongest intensity on the surface did not correspond to the true source position (Fig. 2a2). Based on the single view (Fig. 2a1), we can reconstruct the source in 3D (Fig. 2b1 and b2). The largest CoM deviation between the "true" CBCT and BLT reconstructed positions of the Trigalight is in the depth direction, the Z-axis, at 0.6 mm. The average 3D offset between the true source center and BLT-reconstructed CoM from 4 independent experiments was 0.6 ± 0.1 mm. Comparison of the measured and computed signals at the phantom surface can be found in Figure E3 (available online at www .redjournal.org).

Figure 3 shows the film results for the irradiation based on the source position provided by BLT and CBCT reconstructions in Figure 2. A 0.5-mm-diameter cone and a

5×5 mm^2 square collimator were used for CBCT- and BLT-guided delivery, respectively. In the x- and y-axes, the offsets between the centers of the BLT- and CBCT-guided radiation fields are less than 0.2 mm (Fig. 3b1 and b2). Consistent with the BLT localization result in Figures 2b1 and b2, the largest targeting offset is observed in the lateral view, the z-axis, at 0.6 mm (Fig. 3b2).

Mouse carcass experiments

As observed in the phantom study, the location of the strongest surface BLI of the carcass did not reflect the true source position (Fig. 4a1 and a2). Based on the single AP view (Fig. 4a1), we reconstructed the source in 3D, overlaid on the CBCT image (Fig. 4 b1-b3). The largest CoM
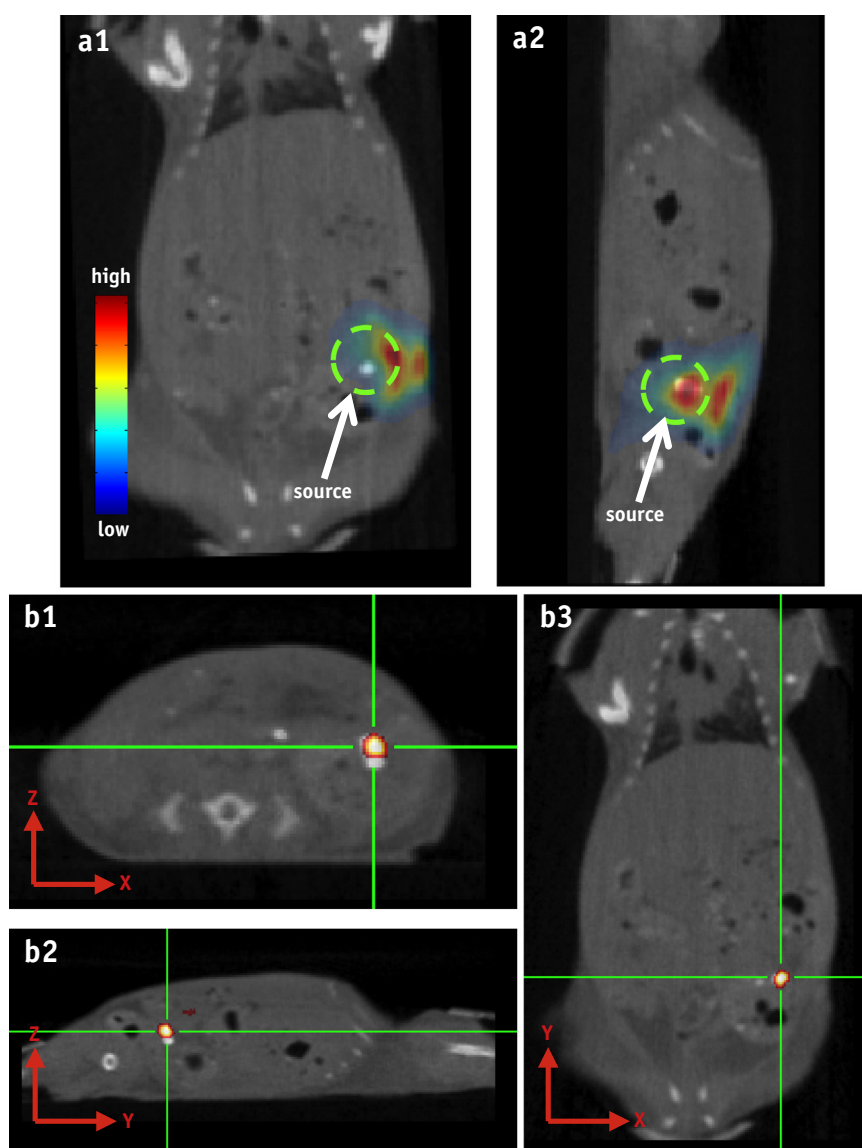

Fig. 4. (a1, a2) AP and lateral BLI overlaid with the CBCT of the mouse carcass implanted with a light source. (b1, b2, b3) Transverse, sagittal, and coronal views of BLT slices overlaid with CBCT. The cross shows the CoM of reconstructed source. Abbreviations are as in Fig. 1 and 2.

deviation of 0.8 mm is in the z-axis (Fig. 4b1 and b2). The average 3D offset between the true source center and BLT-reconstructed CoM from 3 independent carcass experiments was 1.0 ± 0.6 mm. The fit between the measured and computed signals at the mouse surface are shown in Figure E4 (available online at www.redjournal.org). Figure 5 shows the film results of the BLT-guided irradiation compared to results for the CBCT-guided delivery. The targeting difference between the BLT- and CBCT-guided irradiation is minimal in the x- and y-axes (<0.2 mm). The largest deviation of 0.8 mm is clearly seen in the z-axis (Fig. 5b2), consistent with the reconstruction results in Figures 4b1 and b2.

In vivo experiments

Figure 6 shows that the planar BLI can barely separate 2 sources, but BLT can clearly distinguish the sources
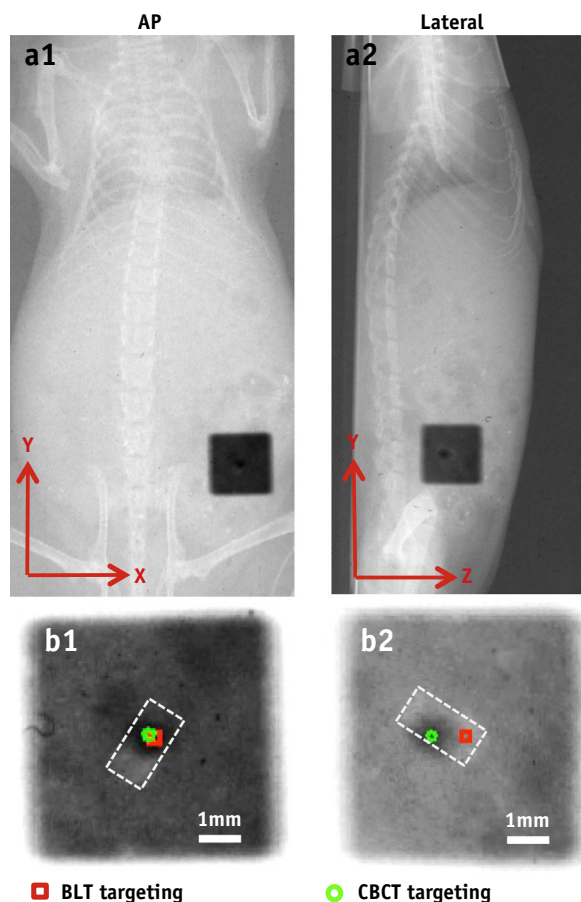

Fig. 5. Film results of target validation in the mouse carcass. The same collimator settings as described in Fig. 3 were used. (a1, a2) Results in AP and lateral views. (b1, b2) Corresponding enlarged views. The true source was contoured by the dashed line. The green circle marks the center of the CBCT guided radiation; the red square marks the center of the BLT-guided radiation. Abbreviations are as in Fig. 1 and 2. Abbreviations as in Fig. 1. A color version of this figure is available at www.redjournal.org.

(Fig. 6a1 vs 6a2). Deviations of the BLT-reconstructed CoM for sources 1 and 2 are 0.8 and 0.9 mm, respectively (Fig. 6a3 and a4). Homogeneous optical properties were assumed in this study, which possibly contributed to the strength of source 1, which was higher than source 2 (Fig. 6a2).

Figure 6b1 shows the surface bioluminescence signal emitted from the subcutaneous tumor. Because cells were located subcutaneously and the tumor was palpable, in this case, the 2D BLI at the tumor surface is believed to represent the tumor location. As we expected, from the top view, the reconstructed 3D bioluminescent distributions (Fig. 6b2, red dots) lie beneath the BLI intensity on the surface (Fig. 6b2). The reconstructed bioluminescence CoM is also within the tumor as shown by CBCT (Fig. 6 b3-b4).

Discussion

Although BLI has been widely used in preclinical research, it has only recently been applied for radiation guidance (42-46). BLI alone is limited in its ability to guide radiation delivery. Recent publications from our group (42, 43) revealed that a vertical beam line directed through the highest bioluminescence surface intensity deviated from the CoM of internal source by as much as 3.5 mm. Due to the irregular phantom and animal surfaces, the optical paths from the bioluminescent source to different surface points can be highly variable such that the location of the strongest BLI signal does not reflect the true source position (Figs. 2 and 4). Weersink et al (46) recently integrated BLI into a X-Rad 225Cx machine (Precision X-ray, North Branford, CT) and asserted that 2D targeting based on BLI in the AP direction can be applied to a single beam or parallel-opposed pair. Their approach alleviates the uncertainty in the depth position of the target, but as can be seen in Figures 2 and 4, the beam margin will need to be quite large to account for the nonintuitive relationship between 2D BLI intensity and the 3D location of the source.

We recently developed a stand-alone CBCT/BLT system (28) for calibration method and algorithm development. In this study, we introduced an online BLT/SARRP system to demonstrate BLT-guided radiation for the first time. Compared with the earlier work from Yang et al (28), this paper integrates multispectral BLT (25, 29), the IVTCG method (30), and permissible source region (31) developed by our group and collaborators to enable fast and accurate CoM reconstruction. Furthermore, the new algorithm enables better conformality of the reconstructed source distributions without a predefined region of interest (compare Fig. 2 in the present study with Fig. 8 in the report by Yang et al [28]). The computation time for our mouse carcass experiments was only 3 minutes using a 64-bit laptop with an Intel Core i7-3920XM 2.9-GHz processor and 32 GB of memory, a time short enough to support online guidance of irradiation. Another positive efficiency factor with our
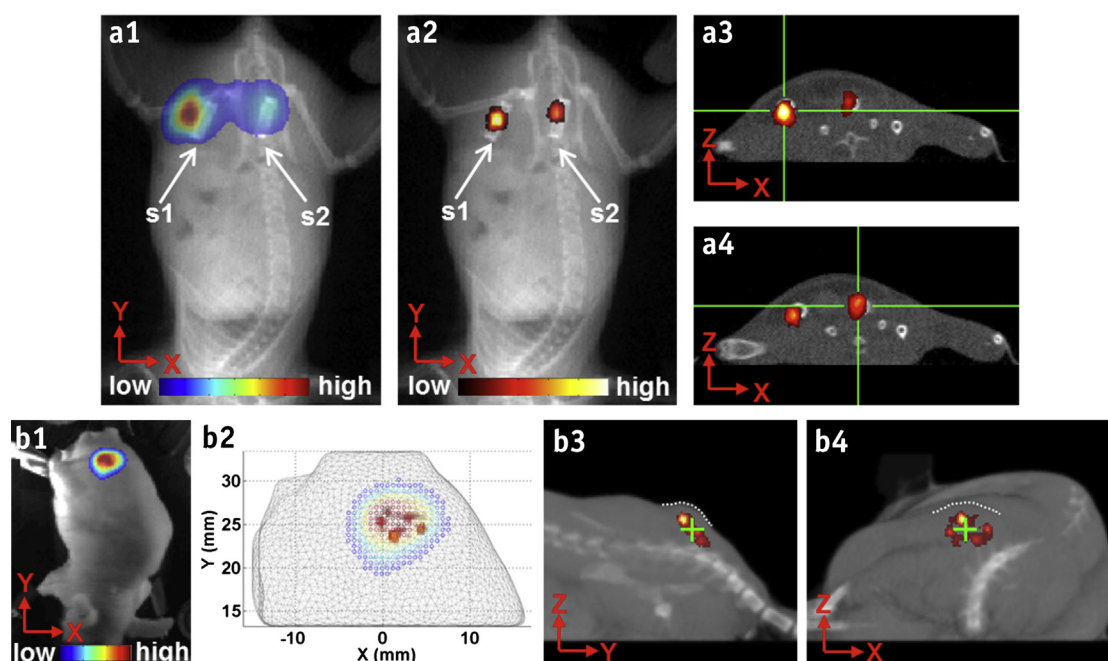
Fig. 6. (a1-a4) Double source experiment: 2 identical cylindrical light sources, source 1 (s1) and source 2 (s2), were implanted in the mouse abdomen. (a1, a2) AP view of BLI at 610 nm and BLT overlapped with CBCT projection, respectively. (a3, a4) Transverse views of the BLT overlapped with CBCT slices for s1 and s2, respectively. The cross denotes the CoM of the reconstructed sources. (b1-b4) In vivo subcutaneous experiment. (b1) BLI overlaid with the photo image; (b2) the top view of BLI overlapped with the BLT reconstructed source onto the mouse mesh; (b3, b4) sagittal and transverse views of BLT overlapped with the 3D rendering of the CBCT. Dashed lines outline the tumor surface, and the cross represents the reconstructed CoM. Abbreviations are as in Fig. 1 and 2.

approach was the use of single-view BLI data for reconstruction. Dehghani et al (25) demonstrated in numerical simulations with a mouse model that spectrally resolved single-view BLT can be used to reconstruct a 2.5-mm radius source within 1-mm accuracy up to 12.5 mm in depth. Although we and others (25) have shown that single-view data can provide excellent BLT reconstruction results, it may explain why our CoM offset was most noticeable in the depth direction. Depth uncertainty can likely be reduced with more camera views, which may also be necessary for metastatic nodules or deep-seated tumors.

Our adoption of the CoM approach is a first step to improve soft tissue targeting. The film validation results show that BLT can be used to guide irradiation of a target based on its CoM which agreed with the CoM derived from CBCT to approximately 1 mm. Once the target CoM is located, our irradiation studies also confirmed that the SARRP can deliver radiation accurately to within 0.2 mm of the target location (13). These capabilities are highly significant for preclinical radiation research involving targets with low CT contrast. Advanced conformal beam arrangements can now be used and would be superior to the limited beam arrangements based on 2D BLI guidance (42-44, 46). The light source used in this study allows direct validation by CBCT, which would not be possible with an actual tumor model. However, in a real-life specimen, the tumor shape can be more complex. Results of our

in vivo studies demonstrate that our BLT system and algorithm have the potential to guide radiation for multiple targets or tumors. The in vivo results for delineating two cylindrical light sources implanted into a live mouse abdomen are promising (Fig. 6 a2-a4), although the results are presented as a cluster of points that emphasizes our algorithm optimized toward CoM reconstruction. A more complete BLT solution, such as higher order radiation transport equation, is expected to provide better target delineation (41, 47). Applying BLT to a subcutaneous model is an initial step toward in vivo image guidance (Fig. 6 b2-b4). Our ultimate goal is to apply BLT guidance to the orthotopic model, which provides a more realistic environment for human cancer study.

In our study, the light source was placed in the abdomen which is a relatively optically homogenous region compared to highly heterogeneous areas such as lung and we selected somewhat preoptimized optical properties for our carcass study. The use of diffuse optical tomography (27) in situ or organ-dependent optical properties will provide a more accurate description of the heterogeneous mouse. We recognize that the current online system requires manual docking. A parallel engineering effort is in progress to provide automated deployment of the BLT system onto the SARRP with better mechanical reproducibility to reduce calibration frequency (48).

Conclusions

In summary, our integrated BLT/SARRP system provides a new opportunity for soft tissue targeting in small animal models with an overall 1-mm targeting accuracy that was achieved in both phantom and mouse carcass models. We also demonstrated the feasibility of applying the BLT-guided system for multiple targets and in vivo tumors.

References

1. Alcorn S, Walker AJ, Gandhi N, et al. Molecularly targeted agents as radiosensitizers in cancer therapy—focus on prostate cancer. *Int J Mol Sci* 2013;14:14800-14832.
2. Kirsch DG. Using genetically engineered mice for radiation research. *Radiat Res* 2011;176:275-279.
3. Zhou H, Rodriguez M, van den Haak F, et al. Development of a micro-computed tomography-based image-guided conformal radiotherapy system for small animals. *Int J Radiat Oncol Biol Phys* 2010; 78:297-305.
4. Wong J, Armour E, Kazanzides P, et al. High-resolution, small animal radiation research platform with x-ray tomographic guidance capabilities. *Int J Radiat Oncol Biol Phys* 2008;71:1591-1599.
5. Tryggestad E, Armour M, Iordachita I, et al. A comprehensive system for dosimetric commissioning and Monte Carlo validation for the small animal radiation research platform. *Phys Med Biol* 2009;54:5341-5357.
6. Clarkson R, Lindsay PE, Ansell S, et al. Characterization of image quality and image-guidance performance of a preclinical microirradiator. *Med Phys* 2011;38:845-856.
7. Stojadinovic S, Low DA, Hope AJ, et al. MicroRT-small animal conformal irradiator. *Med Phys* 2007;34:4706-4716.
8. Graves EE, Zhou H, Chatterjee R, et al. Design and evaluation of a variable aperture collimator for conformal radiotherapy of small animals using a microCT scanner. *Med Phys* 2007;34:4359-4367.
9. Pidikiti R, Stojadinovic S, Speiser M, et al. Dosimetric characterization of an image-guided stereotactic small animal irradiator. *Phys Med Biol* 2011;56:2585-2599.
10. Verhaegen F, Granton P, Tryggestad E. Small animal radiotherapy research platforms. *Phys Med Biol* 2011;56:R55-R83.
11. Tillner F, Thute P, Butof R, et al. Pre-clinical research in small animals using radiotherapy technology—a bidirectional translational approach. *Z Med Phys* 2014;24:335-351.
12. Verhaegen F, van Hoof S, Granton PV, et al. A review of treatment planning for precision image-guided photon beam pre-clinical animal radiation studies. *Z Med Phys* 2014;24:323-334.
13. Matinfar M, Ford E, Iordachita I, et al. Image-guided small animal radiation research platform: Calibration of treatment beam alignment. *Phys Med Biol* 2009;54:891-905.
14. Baumann BC, Benci JL, Santoiemma PP, et al. An integrated method for reproducible and accurate image-guided stereotactic cranial irradiation of brain tumors using the small animal radiation research platform. *Transl Oncol* 2012;5:230-237.
15. Ford EC, Achanta P, Purger D, et al. Localized CT-guided irradiation inhibits neurogenesis in specific regions of the adult mouse brain. *Radiat Res* 2011;175:774-783.
16. Redmond KJ, Achanta P, Grossman SA, et al. A radiotherapy technique to limit dose to neural progenitor cell niches without compromising tumor coverage. *J Neurooncol* 2011;104:579-587.
17. Cunha L, Horvath I, Ferreira S, et al. Preclinical imaging: An essential ally in modern biosciences. *Mol Diagn Ther* 2014;18:153-173.
18. Thorne SH, Contag CH. Using in vivo bioluminescence imaging to shed light on cancer biology. *Proc IEEE* 2005;93:750-762.
19. O'Neill K, Lyons SK, Gallagher WM, et al. Bioluminescent imaging: A critical tool in pre-clinical oncology research. *J Pathol* 2010;220:317-327.
20. Close DM, Xu T, Sayler GS, et al. In vivo bioluminescent imaging (BLI): Noninvasive visualization and interrogation of biological processes in living animals. *Sensors (Basel)* 2011;11:180-206.
21. Contag PR. Whole-animal cellular and molecular imaging to accelerate drug development. *Drug Discov Today* 2002;7:555-562.
22. Ntziachristos V, Ripoll J, Wang LV, et al. Looking and listening to light: The evolution of whole-body photonic imaging. *Nat Biotechnol* 2005;23:313-320.
23. Wang G, Cong W, Durairaj K, et al. In vivo mouse studies with bioluminescence tomography. *Opt Express* 2006;14:7801-7809.
24. Kuo C, Coquoz O, Troy TL, et al. Three-dimensional reconstruction of in vivo bioluminescent sources based on multispectral imaging. *J Biomed Opt* 2007;12:024007.
25. Dehghani H, Davis SC, Pogue BW. Spectrally resolved bioluminescence tomography using the reciprocity approach. *Med Phys* 2008;35: 4863-4871.
26. Darne C, Lu Y, Sevick-Muraca EM. Small animal fluorescence and bioluminescence tomography: A review of approaches, algorithms and technology update. *Phys Med Biol* 2014;59:R1-R64.
27. Naser MA, Patterson MS. Improved bioluminescence and fluorescence reconstruction algorithms using diffuse optical tomography, normalized data, and optimized selection of the permissible source region. *Biomed Opt Express* 2011;2:169-184.
28. Yang Y, Wang KK, Eslami S, et al. Systematic calibration of an integrated x-ray and optical tomography system for preclinical radiation research. *Med Phys* 2015;42:1710.
29. Dehghani H, Davis SC, Jiang S, et al. Spectrally resolved bioluminescence optical tomography. *Opt Lett* 2006;31:365-367.
30. He X, Liang J, Wang X, et al. Sparse reconstruction for quantitative bioluminescence tomography based on the incomplete variables truncated conjugate gradient method. *Opt Express* 2010;18:24825-24841.
31. Naser MA, Patterson MS. Bioluminescence tomography using eigenvectors expansion and iterative solution for the optimized permissible source region. *Biomed Opt Express* 2011;2:3179-3193.
32. Arridge SR. Optical tomography in medical imaging. *Inverse Probl* 1999;15:R41.
33. Dehghani H, Eames ME, Yalavarthy PK, et al. Near infrared optical tomography using NIRFAST: Algorithm for numerical model and image reconstruction. *Commun Numer Methods Eng* 2008;25: 711-732.
34. Cong W, Durairaj K, Wang LV, et al. A born-type approximation method for bioluminescence tomography. *Med Phys* 2006; 33:679-686.
35. Naser MA, Patterson MS. Algorithms for bioluminescence tomography incorporating anatomical information and reconstruction of tissue optical properties. *Biomed Opt Express* 2010;1:512-526.
36. Jermyn M, Ghadyani H, Mastanduno MA, et al. Fast segmentation and high-quality three-dimensional volume mesh creation from medical images for diffuse optical tomography. *J Biomed Opt* 2013; 18:86007.
37. Pekar J, Patterson MS. Fabrication and characterization of phantoms with tissue-like optical properties from 500 to 700 nm. *Med Laser Appl* 2010;25:147-153.
38. Jacques SL. Optical properties of biological tissues: A review. *Phys Med Biol* 2013;58:R37-R61.
39. Alexandrakis G, Rannou FR, Chatziioannou AF. Tomographic bioluminescence imaging by use of a combined optical-PET (OPET) system: A computer simulation feasibility study. *Phys Med Biol* 2005;50: 4225-4241.
40. Virostko J, Powers AC, Jansen ED. Validation of luminescent source reconstruction using single-view spectrally resolved bioluminescence images. *Appl Opt* 2007;46:2540-2547.
41. Klose AD, Beattie BJ, Dehghani H, et al. In vivo bioluminescence tomography with a blocking-off finite-difference SP3 method and MRI/CT coregistration. *Med Phys* 2010;37:329-338.
42. Tuli R, Surmak A, Reyes J, et al. Development of a novel preclinical pancreatic cancer research model: Bioluminescence image-guided

focal irradiation and tumor monitoring of orthotopic xenografts. *Transl Oncol* 2012;5:77-84.

43. Tuli R, Armour M, Surmak A, et al. Accuracy of off-line bioluminescence imaging to localize targets in preclinical radiation research. *Radiat Res* 2013;179:416-421.

44. Lee CJ, Spalding AC, Ben-Josef E, et al. In vivo bioluminescent imaging of irradiated orthotopic pancreatic cancer xenografts in non-obese diabetic-severe combined immunodeficient mice: A novel method for targeting and assaying efficacy of ionizing radiation. *Transl Oncol* 2010;3:153-159.

45. Butterworth KT, Redmond KM, McMahon SJ, et al. Conventional in vivo irradiation procedures are insufficient to accurately determine tumor responses to nonuniform radiation fields. *Int J Radiat Biol* 2015; 91:257-261.

46. Weersink RA, Ansell S, Wang A, et al. Integration of optical imaging with a small animal irradiator. *Med Phys* 2014;41:102701.

47. Klose AD. Multi-spectral luminescence tomography with the simplified spherical harmonics equations. In: Light Scattering Review 7. Berlin: Springer; 2012. p. 37-67.

48. Li M, He X, Eslami S, et al. A dual-use imaging system for preclinical small animal radiation research. In: Jim Patton, editor. Proceedings of the 37th Annual International Conference of the IEEE Engineering in Medicine and Biology Society. New York, NY: IEEE; 2015. p. 6904-6907.